BEHAVIOR AND MODELING OF SHEAR-CRITICAL RC BEAMS UNDER IMPACT LOADING

Selçuk SAATCI and Frank J. VECCHIO

Synopsis: The lack of a complete understanding of shear behavior under high dynamic conditions hindered the efforts for accurate prediction of impact behavior, since severe shear mechanisms may dominate the behavior of RC structures when subjected to impact loads. This current study involves a well-instrumented experimental program that was undertaken to contribute to our understanding of the effects of shear mechanisms on the behavior of reinforced concrete (RC) structures under impact loads. The test results showed that the shear characteristics of the RC beam specimens played an important role in their overall behavior. All specimens, regardless of their shear capacity, developed severe diagonal shear cracks, forming a shear-plug under the impact point. Furthermore, the application of the Disturbed Stress Field Model (DSFM) as an advanced method of modeling shear behavior under impact conditions is also investigated. A two-dimensional nonlinear finite element reinforced concrete analysis program (VecTor2), developed previously for static loads, was modified to include the consideration of dynamic loads such as impacts. VecTor2 analyses of the test specimens were satisfactory in predicting damage levels, and maximum and residual displacements. The methodology employed by VecTor2, based on the DSFM, proved to be successful in predicting the shear-dominant behavior of the specimens under impact.

Keywords: reinforced concrete; shear; impact testing; finite element modeling

ACI member **Selcuk Saatci** is an Assistant Professor at the Izmir Institute of Technology, Izmir, Turkey. He received his BS and MS from the Middle East Technical University, Ankara, Turkey in 1999 and 2001, respectively, and he obtained his Ph.D. degree from the University of Toronto, Toronto, ON, Canada in 2007. His research interests include the nonlinear finite element analysis and impact behavior of reinforced concrete structures.

Frank J. Vecchio, FACI, is a Professor of Civil Engineering at the University of Toronto. He is a member of ACI Committees 441, Reinforced Concrete Columns, and 447, Finite Element Analysis of Concrete Structures. He received the 1998 ACI Structural Research Award and the 1999 ACI Structural Engineering Award. His research interests include advanced constitutive modeling and analysis of reinforced concrete, assessment and rehabilitation of structures, and response under extreme load conditions.

INTRODUCTION

Understanding the mechanisms involved in the impact behavior of reinforced concrete (RC) members and developing methodologies for their analysis and design has been an objective of many researchers and designers. Therefore, numerous analytical and experimental studies have been conducted for this purpose. Experimental studies carried out in this area have revealed that shear mechanisms play an important role in the overall impact behavior of RC structures. Severe shear cracks and deformations, such as shear plugs at the impact location, were observed in the majority of the experimental impact studies. For example, studies carried out by Feldman et al. (1962), Kishi et al. (2002), Ho (2004), and May et al. (2005) reported severe diagonal shear cracks even with statically flexural-critical RC beams tested under impact loads applied at the mid-span.

This paper presents a well-instrumented test program carried out on RC beams, aimed at investigating the role of shear mechanisms on the impact behavior of RC members, as well as providing detailed impact test data that will assist the development and verification of accurate analytical and numerical methods for predicting the impact response. Furthermore, a nonlinear finite element analysis (NLFEA) technique, based on the Disturbed Stress Field Model (DSFM), is introduced for the analysis of the RC structures under impact loads. Data obtained from the test program was used to test this methodology.

Following sections lay out the details of the test program and discusses the major findings. Later, the developed NLFEA technique is explained briefly and the analyses of the test specimens are presented. NLFEA results are compared with the test results and the findings are discussed.

TEST PROGRAM

Eight reinforced concrete beams (four pairs) were constructed as impact specimens for this test program. The dimensions of 250 mm (9.8 in.) width, 410 mm (16.1 in.) height and 4880 mm (192 in.) length were selected. The specimens were tested under simply supported conditions with a shear span of 1500 mm (59 in.), leaving a 940 mm (59 in.) overhang at each end. The overhangs were intended both to amplify the inertia effects on the response, and to obtain fully developed longitudinal bars at the supports.

All specimens had the same amount and configuration of longitudinal reinforcement. They were doubly-reinforced with the longitudinal reinforcement bars placed symmetrically along the height of the specimens, with the intention of having the same member properties in both positive and negative flexure. Canadian Standard No.30 bars, with a 700 mm^2 (1.1 in^2) cross-sectional area and a 29.9 mm (1.18 in.) nominal diameter, were used as longitudinal reinforcement. They were placed as two bars at the bottom and two at the top, spanning the entire length of the specimen. A 38 mm (1.5 in.) clear cover was provided between the top and the bottom beam surfaces and the bars. The transverse reinforcement ratios for the specimens were varied as 0.0%, 0.1%, 0.2% and 0.3%. Closed stirrups were used, which were made from U.S. Standard D-6 deformed wire with a 38.71 mm^2 (0.06 in^2) cross-sectional area and a 7.01 mm (0.276 in.) diameter. Figure 1 presents the details of the test specimens. For easier reference, the specimens were named according to their transverse reinforcement ratio, the only property intentionally varied between the pairs. The transverse reinforcement ratios and stirrup spacing for the specimens are given in Table 1.

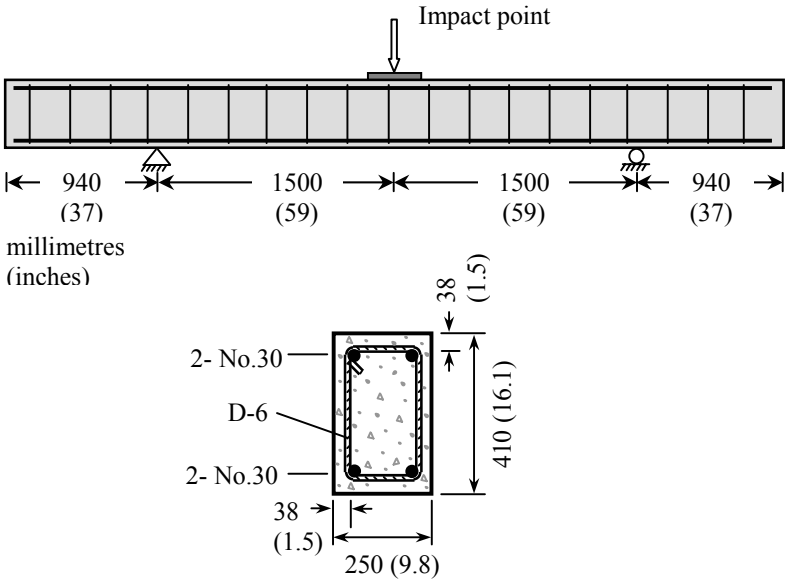

Figure 1 – Specimen dimensions and typical cross-section

Table 1 – Transverse reinforcement ratios and stirrup spacing for the beams

Specimen	Transverse Reinforcement Ratio	Stirrup Spacing mm (in.)
SS0a, SS0b, MS0	0.0%	-
SS1a, SS1b, MS1	0.1%	300 (11.8)
SS2a, SS2b, MS2	0.2%	150 (5.9)
SS3a, SS3b, MS3	0.3%	100 (3.9)

All of the specimens were tested under the same simply supported conditions. Uplift of specimens at the supports was prevented by holding down the beam with No.30 reinforcement bars (see Figure 2). The bars were threaded at both ends and bolted at the top end to a hollow structural steel (HSS) section, which crossed the specimen in width. The bars were fitted with strain gauges and calibrated under tension, so that by measuring their strains it would be possible to calculate the force they carry. At the bottom end, in order to enable free-rotation, the bars were fitted to spherical bearings which were supported by steel floor beams bolted to the strong floor. Between the specimen and the HSS section at the top, a hinge was placed. With this setup, the specimens were able to rotate freely with minimal secondary moments at the supports.

Four additional specimens were cast to determine the static behavior of the specimens tested under impact loading. Each static specimen had an identical reinforcement layout as its corresponding impact specimen; these beams were denoted with "MS", followed by the specimen type number. Impact and static specimens having the same specimen type number had the identical reinforcement layout (e.g. SS2a and SS2b had identical reinforcement layout with MS2). All static specimens were cast at the same time using the same concrete batch; therefore, all had an identical concrete strength, close to the average concrete strength attained in the impact specimens.

The concrete used for the specimens was obtained from a local ready-mix concrete company. A 10 mm (0.4 in.) maximum aggregate size and 100 mm (3.9 in.) slump was specified in the order. The specimens were cast two at a time and both specimens were cast from a single batch. During the casting, several standard cylinder samples (150 mm [6 in.] in diameter and 300 mm [12 in.] in height) were taken to determine the compressive strength of the concrete. To determine the properties of the steel reinforcement, standard tensile coupon tests were carried out. Stress-strain curves obtained both from concrete cylinder tests and steel coupon tests are presented in Figure 3.

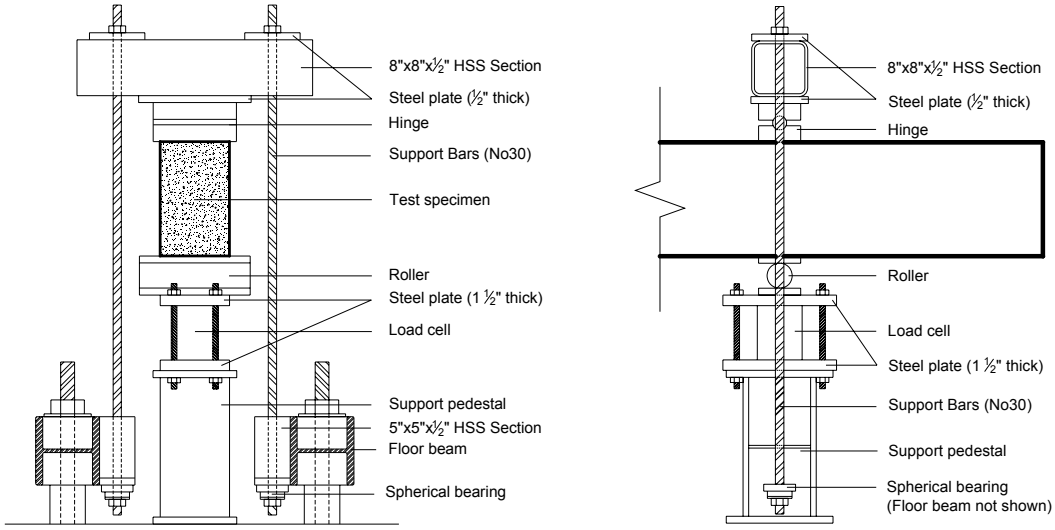

Figure 2 – Test setup details at the supports

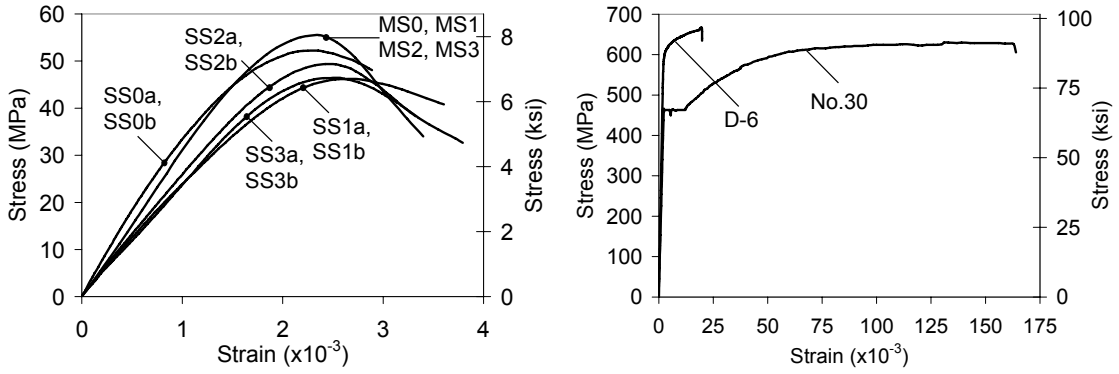

(a) Concrete cylinder responses (b) Steel bar coupon responses

Figure 3 – Stress-strain response for concrete and steel bars

The impact specimens in this test program were well-instrumented. Seven accelerometers were used for each test; five were mounted on the specimen to measure the accelerations during the impact-induced vibrations, and two were mounted on the drop-weight to characterize the impact force. Fifteen potentiometers were attached along the bottom surface of the specimen, at regular intervals, to measure vertical displacements (see Figure 4). All longitudinal bars were fitted with electrical-resistance strain gauges, applied at three different locations. Three stirrups in each beam were also fitted with the same type of strain gauges. Two load cells were used at the supports to measure the reaction forces. The data collected were captured at a 2.4 kHz sampling rate by a digital data acquisition system.

Two different drop-weights were used for the testing; a lighter weight of 211 kg (465 lb) and a heavier weight of 600 kg (1323 lb). They were manufactured by filling a 300 mm square HSS section with concrete. The heavier drop-weight had additional thick steel plates welded on both sides of the HSS section for extra mass. Both drop-weights were 304 mm (2 feet) in length and had a hook at the top. They were fitted with two accelerometers to calculate the impact force. Impact loads were applied via the free-fall of the drop-weights impacting the specimens at the mid-span. The contact surfaces of the drop-weights were flat, and a 50 mm (2 in.) thick, 305 mm (12 in.) square steel plate was placed on top of the beam at impact point to obtain a well-distributed impact force. For all impact tests, the weights were dropped from a clear height of 3.26 m (128.3 in.) above the specimen, resulting in an 8.0 m/s (26.25 feet/s) calculated impact velocity. All specimens, except SS0b, were tested more than once. With the a-series specimens, the beams were tested

once with the 211 kg drop-weight first, then twice with the 600 kg weight. For b-series specimens, the order was reversed; they were tested twice with the 600 kg drop-weight first, and then once with the 211 kg weight. Using this procedure, the total impact energy imparted to the specimens was kept constant between twin specimens, except for those that failed prior to the second or third impact (SS0a and SS1b were tested twice, and SS0b was tested only once). This arrangement of delivering the impact energy was intended to observe the effect of previous damage on the resistance characteristics of the specimens.

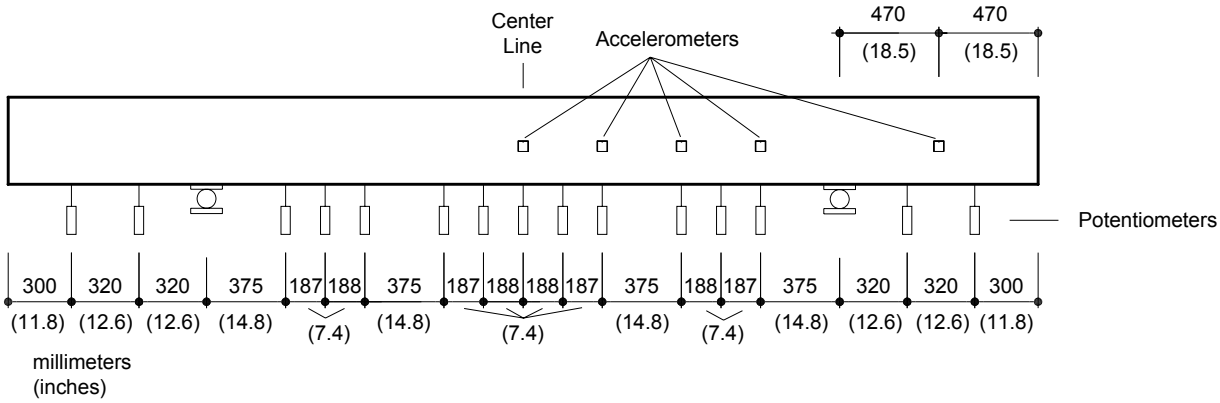

Figure 4 – Accelerometer and potentiometer locations

After the completion of the impact test program, the corresponding static specimens were tested under monotonically increasing static loads to determine their static capacity and behavior. These specimens were loaded at the mid-span, with support conditions identical to those used with the impact tests. Further details of the entire test program can be found at Saatci (2007) and Saatci and Vecchio (2009a).

TEST RESULTS AND DISCUSSIONS

Static Test Results

The mid-span load-deflection responses obtained from static tests are presented in Figure 5. Specimens MS0 and MS1 failed in a shear-critical mode with the formation of a principal diagonal shear crack, whereas MS2 and MS3 exhibited a ductile flexural response. Table 2 presents the maximum reaction forces measured during the static tests for each specimen.

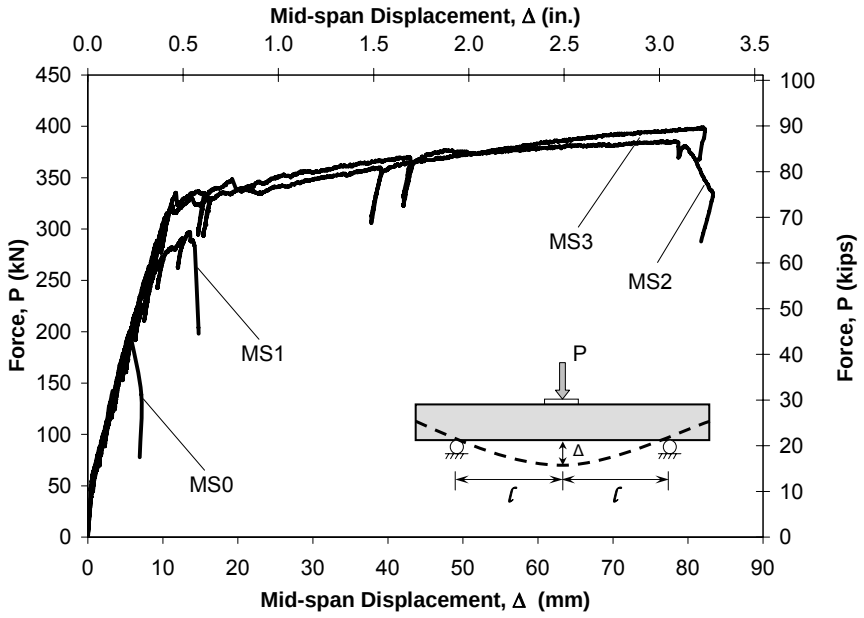

Figure 5 – Static response of test specimens

Table 2 - Static capacities of test specimens

Specimen	Maximum Static Reaction Force* kN (kips)	Failure Mode
MS3 (SS3a, SS3b)	199 (45)	Flexural
MS2 (SS2a, SS2b)	193 (43)	Flexural
MS1 (SS1a, SS1b)	149 (33)	Shear
MS0 (SS0a, SS0b)	98 (22)	Shear

* Maximum applied mid-span load divided by 2.

Impact Test Results

Data collected by the sensors were recorded using a high-speed digital data acquisition system. The mid-span displacements and support reactions (measured at one support) are presented in Figure 6 and 7, for the first impacts on a- and b-series specimens, respectively (note that the results for SS0b-1 are omitted since the data were not reliable due to extensive damage). In addition, after each test, the cracks developed were marked, and their widths were measured. Figure 8 and 9 present the sketches of the crack maps of the specimens at their final stage (after the multiple impact tests). The complete test data obtained from the sensors are available in digital format at the University of Toronto - VecTor Analysis Group website (see References). Detailed reports on the individual tests and complete crack maps can be at Saatci (2007).

The following sections summarize and discuss the main observations made during the impact tests. In the notation used to denote the impact tests, the number following the specimen name indicates the sequence of the particular test performed on that specimen.

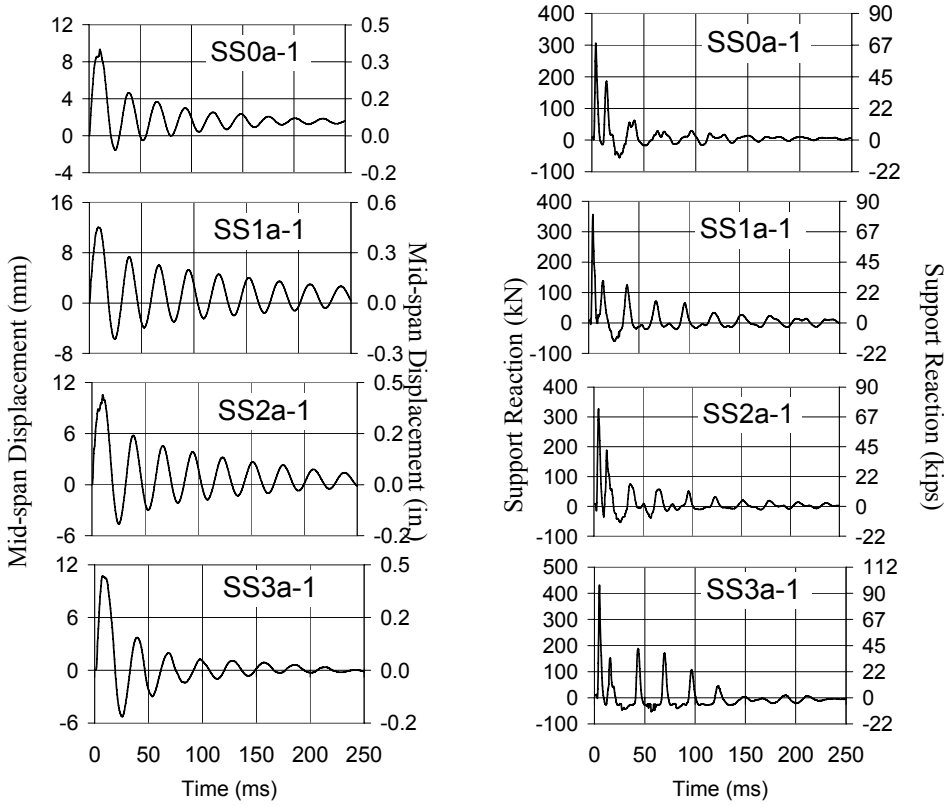

Figure 6 – Mid-span displacements and support reactions for a-series specimens (first impact)

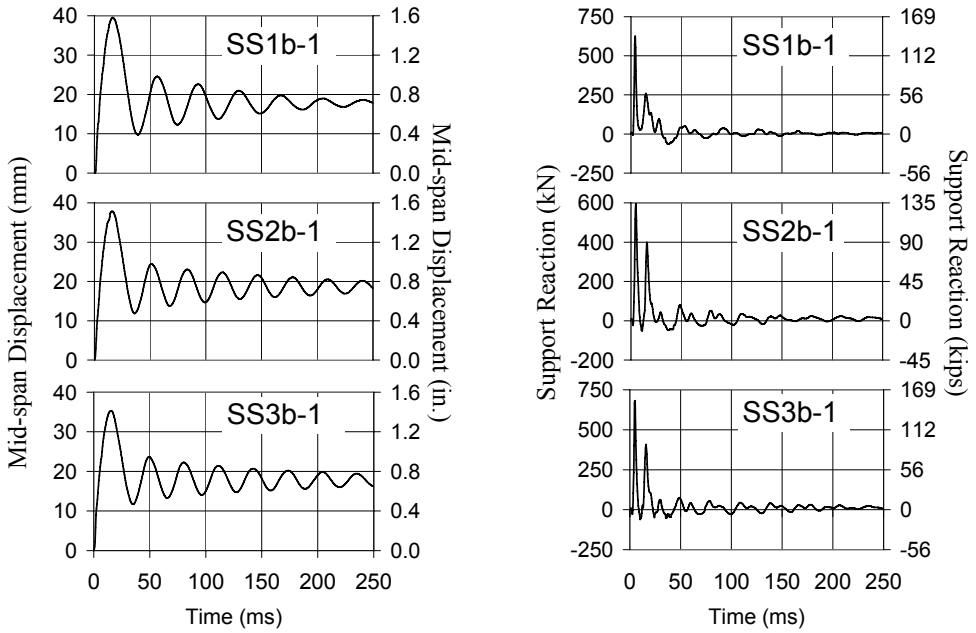

Figure 7 – Mid-span displacements and support reactions for b-series specimens (first impact)

Crack Patterns

The static test conducted on the duplicates of the impact specimens revealed that SS3 and SS2 experience a ductile flexure-critical behavior, whereas SS1 and SS0 are shear-critical, under static loading. However, during the impact testing, regardless of their static behavior, all specimens developed severe diagonal cracks, starting from the impact point and propagating downwards with an angle of approximately 45 degrees, forming shear-plugs. In addition, several diagonal cracks parallel to the major shear-plug cracks also developed, along with some flexural cracks at the mid-span and at the supports. These flexural cracks usually propagated vertically through the height of the beams, although the vertical cracks at the mid-span started from the bottom surface and the cracks at the supports started from the top surface. Several other short vertical cracks, starting from the top of the specimens, were also observed in most of the specimens due to negative bending moments at the initial stages of the impact.

The crack patterns and failure modes varied between specimens depending on their static capacities. For example, in the flexure-critical specimens, SS2 and SS3, flexural cracks at the mid-span were more visible and wider, whereas they were shorter and narrower in SS1 and SS0. In SS2 and SS3, subsequent impacts on the damaged specimens did not change the widths of the cracks located beyond the major diagonal cracks forming the shear-plug; increasing deformations were mostly accommodated by the widening of shear cracks forming the shear-plug. However, in SS1 and SS0, another diagonal crack developed alongside the shear-plug, starting from the supports, propagating at an angle of approximately 45 degrees upwards, and becoming horizontal close to the top before reaching to the impact zone (see Figure 10). These cracks were quite similar in nature to the typical shear cracks that result in failure of shear-critical beams under static loads, and they became wider with subsequent impacts, causing the failure of the specimens in SS1a-3, SS0a-2, SS1b-2 and SS0b-1.

Typical crack widths measured after each test are summarized in Table 3. Note that the damage was not always symmetric on both sides of the specimens; therefore, the crack widths in Table 3 are the maximum values. Some cracks were either not measured or it was not possible to measure them due to extensive spalling; such cases are denoted by a question mark.

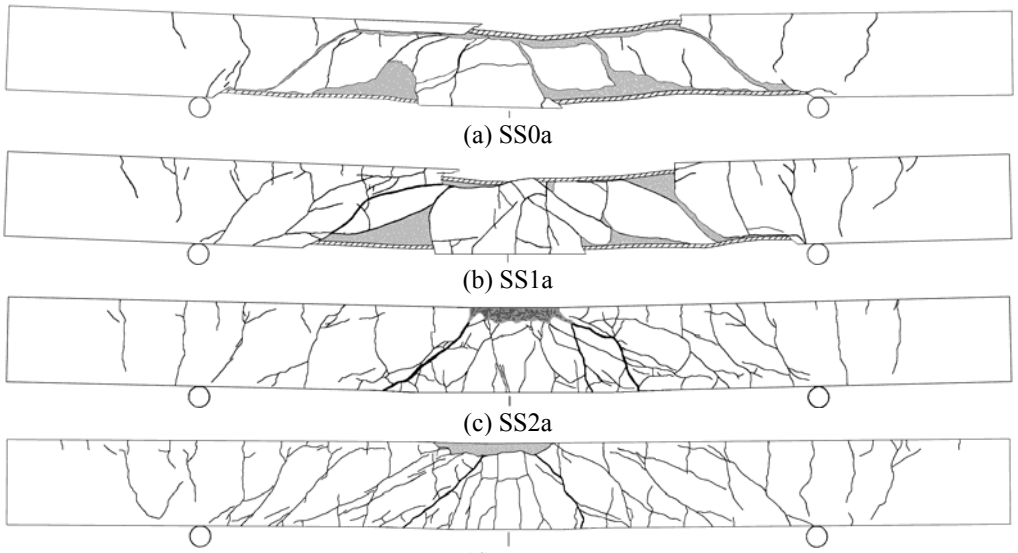

(a) SS0a

(b) SS1a

(c) SS2a

(d) SS3a

Figure 8 – Final crack profiles for a-series specimens

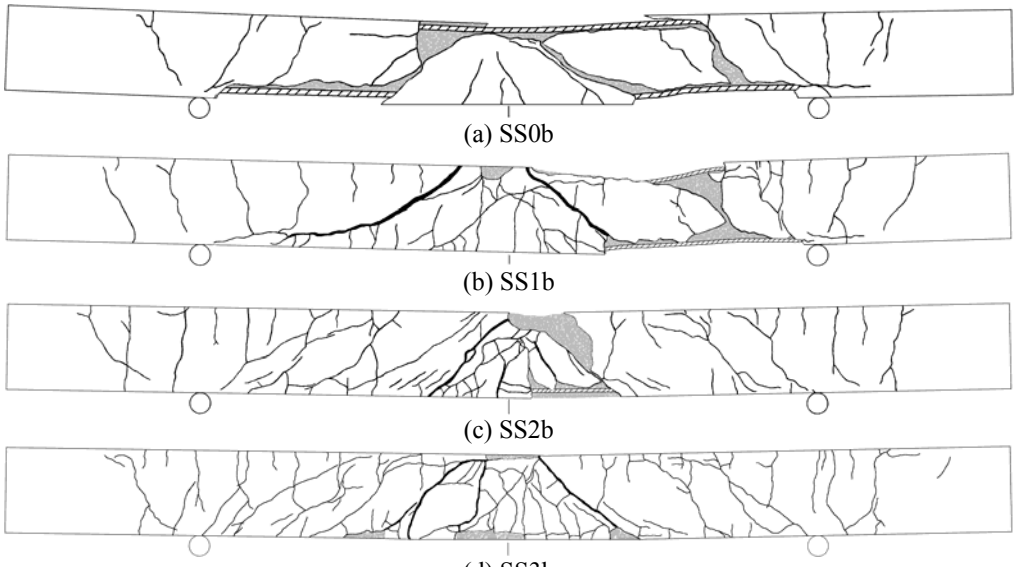

(a) SS0b

(b) SS1b

(c) SS2b

(d) SS3b

Figure 9 - Final crack profiles for b-series specimens

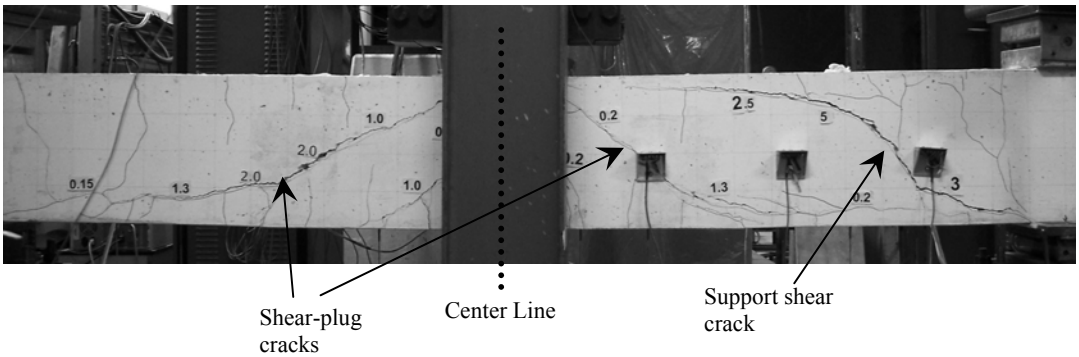

Figure 10 – Typical cracks in a shear-critical specimen (SS1b-1)

Table 3 - Typical crack widths measured after tests

Test	Diagonal crack width (shear-plug) mm (in.)	Flexural crack width (mid-span) mm (in.)	Support shear crack width mm (in.)	Test	Diagonal crack width (shear-plug) mm (in.)	Flexural crack width (mid-span) mm (in.)	Support shear crack width mm (in.)
SS3a-1	0.15 (0.01)	?	-	SS3b-1	0.50 (0.02)	1.00 (0.04)	0.10 (0.004)
SS3a-2	1.10 (0.04)	1.30 (0.05)	0.25 (0.01)	SS3b-2	2.00 (0.08)	2.00 (0.08)	0.20 (0.01)
SS3a-3	1.80 (0.07)	?	0.40 (0.02)	SS3b-3	?	2.00 (0.08)	0.20 (0.01)
SS2a-1	0.20 (0.01)	< 0.10 (0.004)	-	SS2b-1	1.80 (0.07)	1.10 (0.04)	0.20 (0.01)
SS2a-2	3.00 (0.12)	1.80 (0.07)	0.20 (0.01)	SS2b-2	2.00 (0.08)	1.80 (0.07)	0.20 (0.01)
SS2a-3	5.00 (0.20)	1.80 (0.07)	0.20 (0.01)	SS2b-3	> 10.00 (0.40)	1.80 (0.07)	0.20 (0.01)
SS1a-1	0.30 (0.01)	-	0.20 (0.01)	SS1b-1	2.00 (0.08)	0.90 (0.04)	5.00 (0.20)
SS1a-2	3.50 (0.14)	0.60 (0.02)	4.00 (0.16)	SS1b-2	5.00 (0.20)	0.90 (0.04)	> 10.00 (0.40)
SS1a-3	?	0.60 (0.02)	> 10.00 (0.40)	SS1b-3		Not conducted	
SS0a-1	0.20 (0.01)	-	0.50 (0.02)	SS0b-1	> 10.00 (0.40)	< 0.10 (0.004)	> 10.00 (0.40)
SS0a-2	> 10.00 (0.40)	-	>10.00 (0.40)	SS0b-2		Not conducted	
SS0a-3		Not conducted		SS0b-3		Not conducted	

Observations made from the development of crack profiles and crack widths revealed that the failure modes were determined mainly by the static behavior of the specimens. In the flexure-critical specimens, shear-plugs developed faster than did the support shear cracks. Their capacities were higher, comparing the damage they suffered to the damage shear-critical specimens suffered, after three impacts. Although they developed pronounced shear-plugs as well, failure of the shear-critical specimens was not entirely a result of the shear-plugs, but rather the shear failure at the supports. In other words, the shear strengths of flexure-critical specimens were sufficient to carry the shear forces beyond the shear-plug to the supports; subsequent impacts pushed the shear-plug down further, without creating significant damage in the rest of the specimen. However, this was not the case for shear-critical members. These specimens did not have sufficient strength to transmit the shear forces to the supports. Consequently, the shear forces beyond the shear-plug caused extensive damage between the shear-plug and the supports, ultimately failing the beam in this segment. In any case, the flexural behavior of all specimens was minimal. The flexure-critical beams developed some wide vertical cracks, but their widths were always less than the width of the diagonal shear cracks. Since the deformations caused by the shear-plugs dominated the displacement profile, the shear-critical specimens developed much narrower flexural cracks.

Displaced Shape

As mentioned before, displacement sensors were connected to the specimen along the bottom face, measuring the displacements at 15 different locations. Assuming zero displacement at the supports, and extrapolating the end displacements by using the slope of the overhanging parts, the displaced shape of the specimens can be obtained for each sampling time. These shapes, obtained up to the first peak of the vibrations, are presented in Figure 11 for the first impacts on b-series specimens. For SS0b-1, since most of the displacement sensors were disconnected from the specimen due to excessive concrete spalling, only about the first 20 ms of displacement response were captured successfully.

It can be seen that the middle three displacements are very close in all tests, indicating the motion of the shear-plug. This behavior is less apparent in the specimen with the highest stirrup ratio, SS3b, since the stirrups significantly reinforced the specimen against shear, allowing the bending of the middle segment to a certain degree. In SS1b, on the other hand, there was notably less bending in the middle segment, evidenced by the comparable displacements recorded by the middle five sensors. SS0b had no stirrups, hence the middle segment punched through with almost no visible bending deformations; the shear-plug formation can be observed clearly in the displaced shape.

Dynamic Equilibrium

When a drop-weight impacts a specimen, the resulting impact force is resisted by the stiffness of the specimen, while the specimen accelerates in the direction of the impact force. The acceleration of the specimen creates inertia forces, equal in magnitude to the mass times acceleration. If the direction of these inertia forces is taken as opposite to the direction of the accelerations, a state of force equilibrium can be established for that point in time, which is referred to as *D'Alembert's principle of dynamic equilibrium* (Chopra 2001). Ignoring the damping forces, a free body diagram for this state of dynamic equilibrium can be derived as shown in Figure 12 for the test specimens.

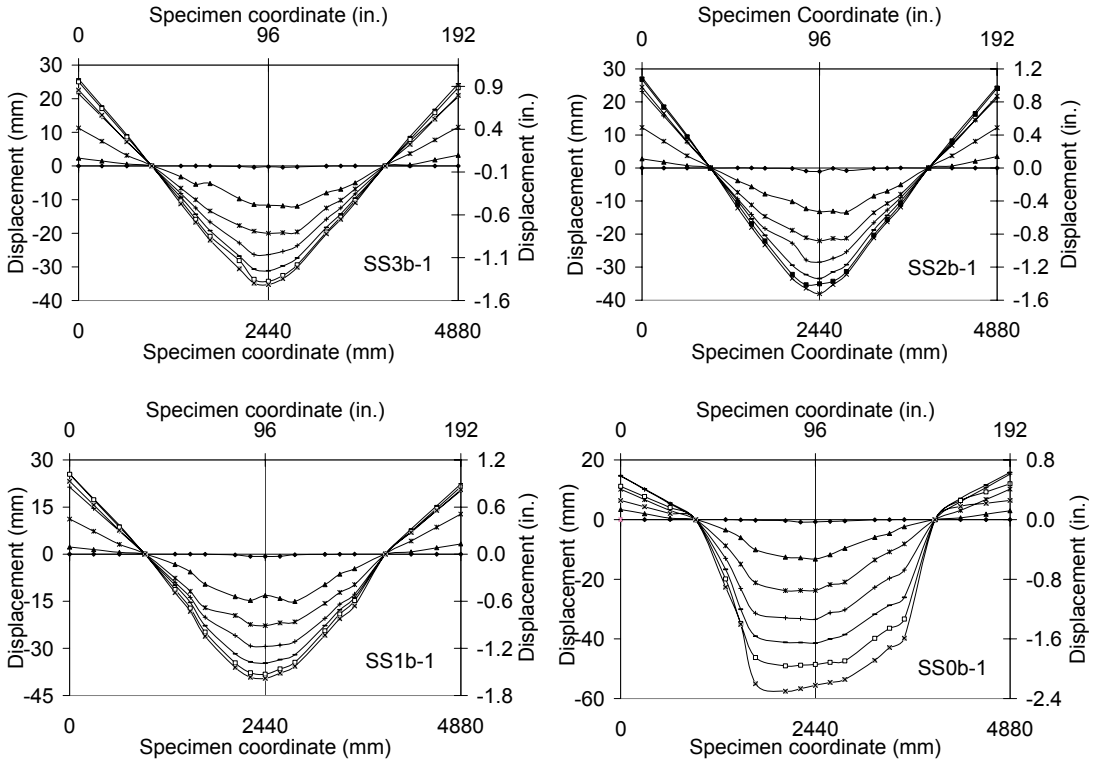

Figure 11 - Displaced shapes (2.50 ms intervals)

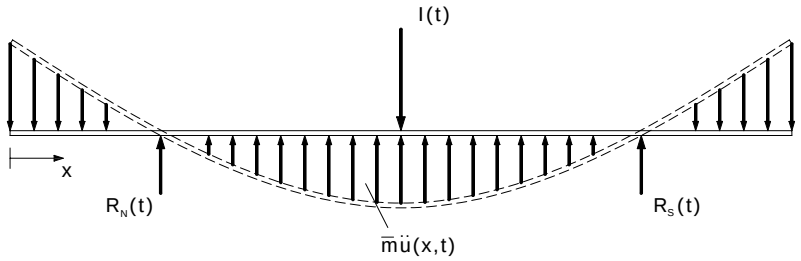

Figure 12 - Dynamic free body diagram for the test specimens

In Figure 12, I(t) is the impact force, $\overline{m}$ is the mass per unit length, $\ddot{u}(x,t)$ is the acceleration of the specimen, and $R_N(t)$ and $R_S(t)$ are the support reaction forces at the north and south supports, respectively. According to this free body diagram, the vertical force equilibrium of the specimen at any time t can be expressed as follows:

$$\int_0^L \overline{m}\ddot{u}(x,t)dx + R_N(t) + R_S(t) - I(t) = 0 \qquad (1)$$

where L is the total length of the specimen. In this test program, all quantities in Eq. 1 were measured during the tests, providing an opportunity to verify the test data for dynamic equilibrium and examine the corresponding behavior of the specimens. As mentioned before, the accelerations on the specimen were measured by accelerometers attached to one half of the specimen at five different locations. The support reactions $R_N(t)$ and $R_S(t)$ were obtained from the load cell readings. The impact forces I(t) were calculated as the product of the accelerations of the drop-weight multiplied by its mass. After obtaining all the required terms, the dynamic equilibrium in Eq. 1 was checked for the test specimens. As a representative case, the variation of forces in SS3a-1 is presented in Figure 13. As seen in the figure, the peak impact

and resisting forces exhibited an almost perfect match for SS3a-1. After the peak, the resisting forces exhibited some fluctuations, whereas the drop-weight bounced back and lost contact with the specimen. From an equilibrium point of view, although the specimens continued to vibrate, such fluctuations in the sum of forces should not have existed since the inertia forces should have cancelled out with the reaction forces for the case where I(t) is equal to zero. These fluctuations were thought to be mostly a result of measurement errors, since noise in the system, both electrical and physical, such as that caused by cracking and spalling of concrete, were registered in the accelerometers and load cells as unrealistic readings. The effects of these factors diminished in later stages and the sum of resisting forces dropped to zero as expected.

A further investigation, similar to the one described by CEB (1988), can reveal more about the distribution of forces along the specimen. As stated in Eq. 1, the impact force is resisted by a combination of inertia and reaction forces. The distribution of these forces, and the resulting shear and moment distributions, can be determined by using the basic principles of static equilibrium, as shown in Figure 14.

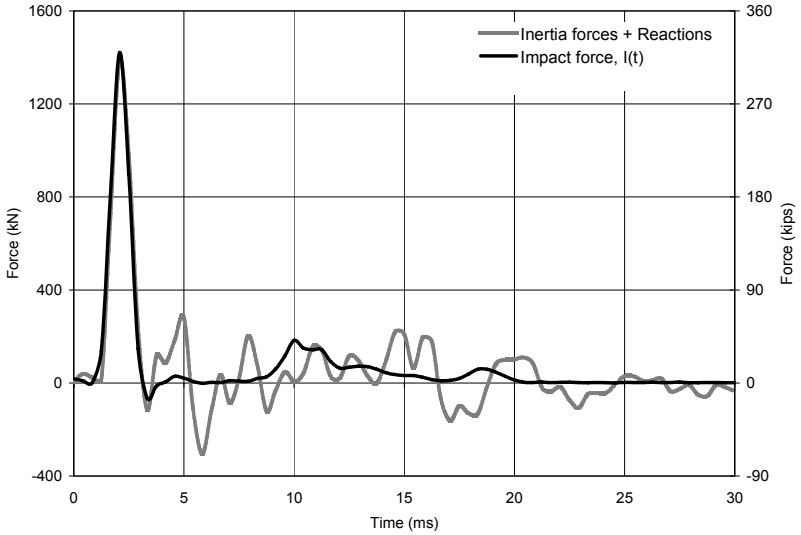

Figure 13 - Dynamic equilibrium of forces, SS3a-1

In Figure 14, a is the length of the overhang, *l* is the shear span, I is the impact force, and α is the ratio of the inertia forces to the total impact force. The inertia force distribution is assumed proportional to the elastic displaced shape. The total reaction force at the supports can be found as follows:

$$R = (1-\alpha)\frac{I}{2} \qquad (2)$$

which can be checked against the test results, to find the value of α. In SS3a-1, for example, where the peak resisting forces and the impact force were in almost perfect agreement, the peak impact force was 1421 kN (319 kips) and the average peak support reaction at the same point in time was 13.1 kN (3 kips), giving $\alpha = 0.98$. The same calculations done for other tests also gave α values close to 1.0 for the first peak, meaning that almost all the impact force was resisted by the inertia forces at the first instant, before it was transmitted to the supports. This can be seen more clearly when the resisting forces are broken down to their components, as done in Figure 15 for SS3a-1.

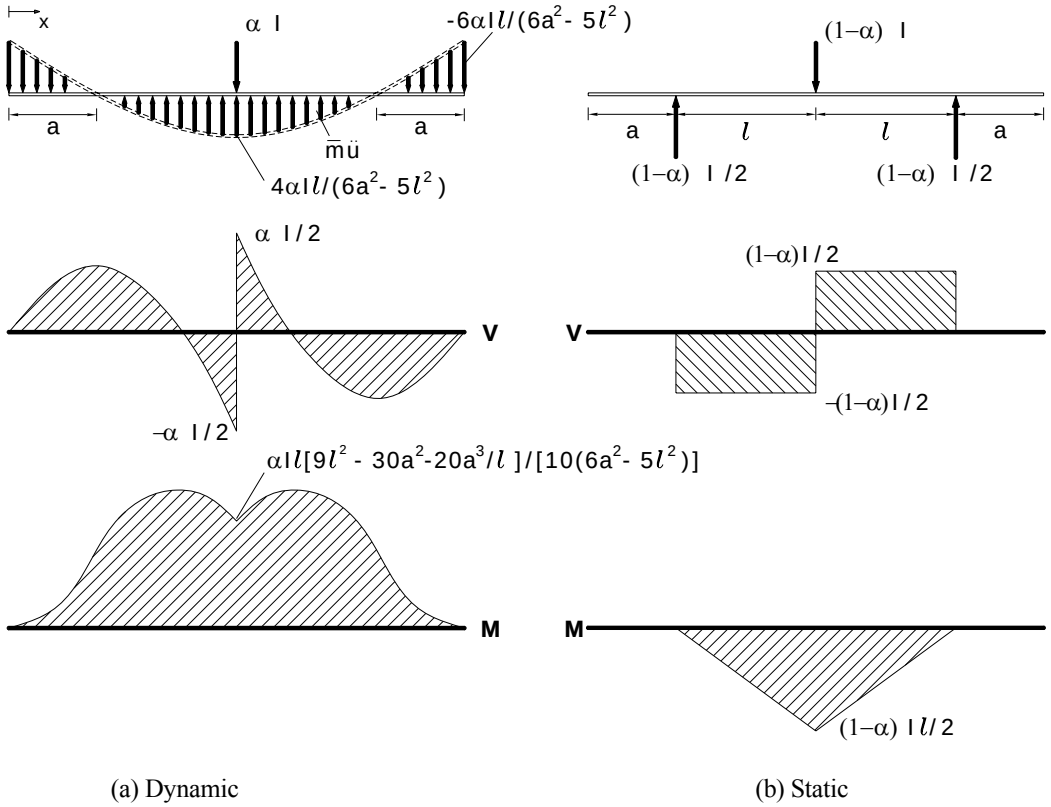

Figure 14 - Distribution of forces

This phenomenon also explains the formation of the shear-plug. As seen in the moment diagrams in Figure 14, the mid-span moment for the case of α = 1.0 is much smaller than it is for the static case of α = 0.0. If values of a=0.94 m and l = 1.5 m are substituted, it can be found that the maximum moment for α = 1.0 is 0.437 I, whereas for α = 0.0, it is 0.75 I. However, the mid-span shear force is independent of α, always equal to I/2. Therefore, in the initial stages of the response, the specimen experiences the same shear force but significantly smaller moments than it would under static loading, thus becoming shear-critical, forming the diagonal shear cracks and the subsequent shear-plug.

Another consequence of α being close to 1.0 in the initial stages of the response is the vertical cracks observed along the specimen. As seen in the moment diagram presented in Figure 13, α = 1.0 creates negative moments along the entire length of the specimen. These negative moments resulted in vertical cracks starting from the top and propagating downwards (see Figure 16). Typically, these cracks were spaced closer on the specimens with higher stirrup ratio compared to the specimens with larger stirrup spacing. They were characterized by narrow crack widths (usually around 0.10 mm), since they formed in the very early stages of the response and closed quickly after the negative moments diminished, i.e. as the α-value approached zero. Vertical cracks developed at the overhanging parts as well; however, they had an inclination towards the supports as they propagate downwards, due to the high shear forces at the supports along with negative moments when α = 1.0 (see Figure 17).

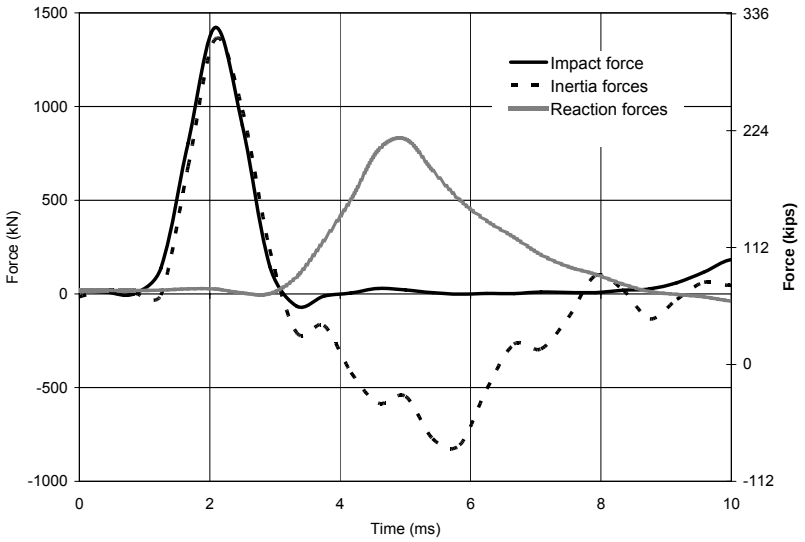

Figure 15 - Breakdown of resisting forces, SS3a-1

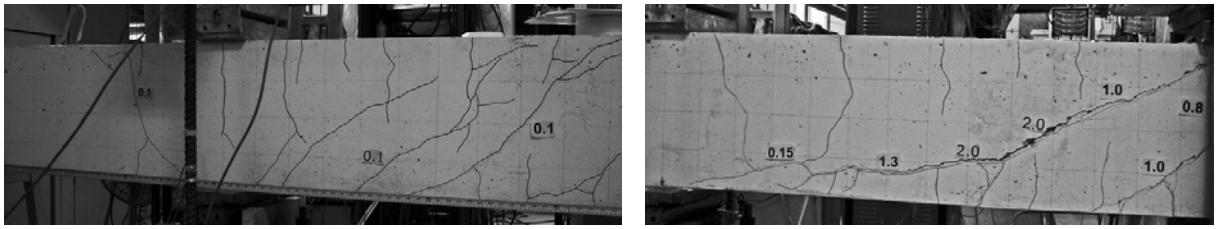

(a) SS3b-1 (b) SS1b-1

Figure 16 - Vertical cracks due to negative moments

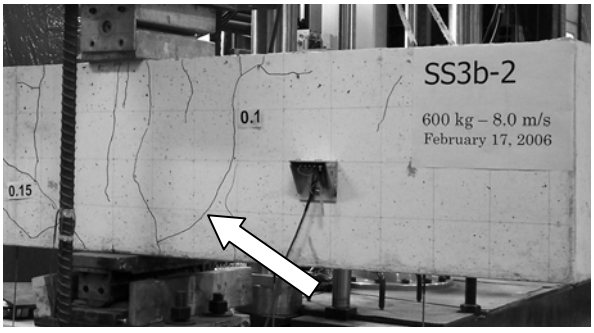

Figure 17 - Inclination of a vertical crack at the overhanging part

FINITE ELEMENT MODELING

For this study, the NLFEA procedure implemented into the two-dimensional, nonlinear finite element analysis program for reinforced concrete, VecTor2 (Vecchio and Wong 2002), was modified to include the impact loads. VecTor2, developed previously at the University of Toronto, is based on the Disturbed Stress Field Model (DSFM) and follows a rotating smeared-crack approach for modeling reinforced concrete (Vecchio 2000). The program employs simple techniques for finite element modeling, using low order 4-node rectangular, 4-node quadratic, or 3-node triangular

elements for modeling reinforced concrete, while concentrating on the utilization of a wide array of advanced constitutive and behavioral models for concrete and steel reinforcement.

The dynamic loads were introduced in VecTor2 through an implementation of a time-stepping algorithm. Newmark's Method of Direct Integration (Newmark 1959) was re-formulated for secant stiffness approach employed by DSFM. A lumped mass matrix was implemented to represent the mass of the structure. Although the major energy dissipating mechanisms, such as material hysteresis and concrete cracking, can be included in the nonlinear formulations of DSFM through the material and behavioral models employed, a small amount of viscous damping was found necessary for numerical stability of the solutions, and was incorporated using *Rayleigh damping* (Chopra 2001). The stiffness formulation of DSFM, already present in the program, was used for representing the stiffness. The details of the direct integration method and the analysis algorithm can be found in Saatci and Vecchio (2009b).

Impact test on the test specimens were modeled using the newly developed NLFEA procedure. A total of 1008 rectangular elements were used to represent the concrete, the drop-weight and the support plates, and 124 truss bar elements were used to model the longitudinal steel reinforcement (see Figure 18). The mesh included 1098 nodes. Taking advantage of the symmetric load and support conditions, only one-half of a beam was modeled. All nodes at the centerline of the beam were restrained against translations in the y-direction. The mesh size was optimized through a parametric study investigating finer and coarser meshes.

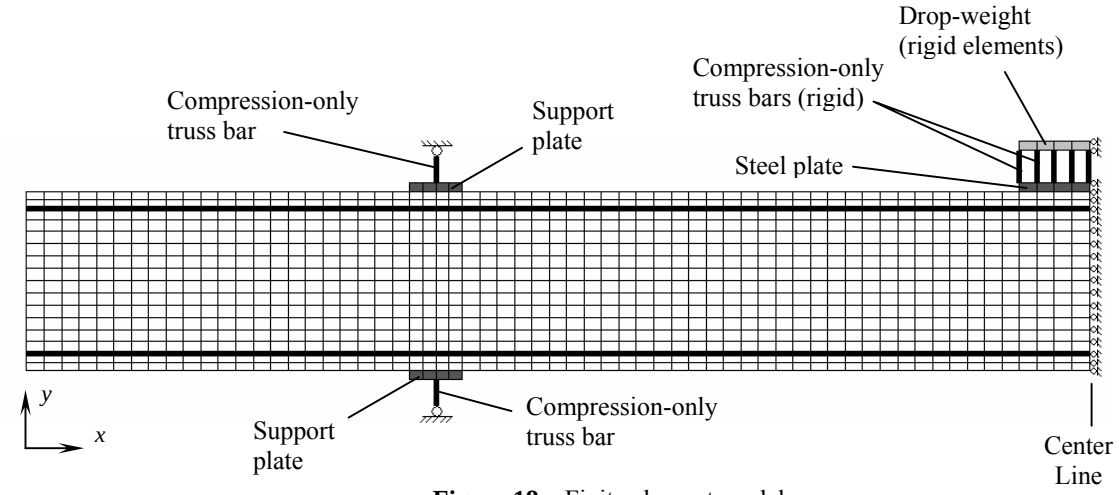

Figure 18 – Finite element model

The 150 mm wide steel bearing plates at the supports were modeled with four elements placed at the top and bottom support points. As mentioned before, the specimens were restrained against upward movements at the supports by No.30 bars, which held the specimen down from the top. To simulate these conditions, supports were introduced in the model with compression-only truss bars connected to the elements representing the support plates at one end, and fixed against translations at the other end. With this arrangement, uplift forces were supported by the top truss bar, avoiding any artificial tensile stresses in the specimen that would occur if the bottom support was restrained against translations in y-direction. These truss bars were assigned calculated stiffness properties to simulate the actual stiffness of the supports in the tests. The drop-weight was modeled using four rigid rectangular elements, each 40 x 20 mm in size. The stiffness properties of these elements were assigned very high values to ensure a rigid behavior. The elements modeling the drop-weight were connected to the specimen by five compression-only truss bars, so that when the drop-weight bounced back, it would not pull up on the specimen. These truss bars were also assigned very high stiffness properties, and they were connected to the elements representing the steel plate placed at the point of impact. The transverse steel reinforcement was modeled as smeared within the concrete, since the stirrups provided were regularly distributed along the specimen. The longitudinal steel reinforcement was modeled with 124 truss bars. Each truss bar element was directly connected to concrete elements; that is, perfect bond was assumed.

The Popovics (1973) formulation for normal strength concrete was selected as the compression base curve, since it was found to best fit the stress-strain curve obtained from the tests of the cylinder specimens. The model proposed by Palermo and Vecchio (2002) was used to model the hysteretic response of concrete. All other material and behavioral models used for concrete and steel were the default models of VecTor2. Details on the formulations of these models can be found in the VecTor2 and Formworks Manual (2002). It has to be noted that the material models have not been modified to include strain rate effects, considering the uncertainties involved. A more detailed discussion on this issue can be found in Saatci and Vecchio (2009b).

The masses of the rectangular concrete elements were equally divided into four and assigned to their nodes. Similarly, the masses of the truss bars were divided into two and added to the corresponding nodal masses. The half-mass of the drop-weight was equally distributed among its nodes, and the time-stepping algorithm was initiated by assigning the contact velocity of the drop-weight to these nodal masses. Much of the damping mechanism was inherently included in the material models (i.e., through hysteresis and cracking); thus, the amount of viscous damping needed for numerical stability was determined through parametric study by reducing the viscous damping ratio successively until the solution lost its stability. The minimum amount of viscous damping required varied between 0.5 to 1% of critical damping, assigned to the first and second modes of vibration. Only for specimens which suffered heavy damage, a higher damping ratio, up to 5%, was needed for solution stability. In all analysis, the constant acceleration method was used. As the result of further parametric studies, a time step of 0.1 milliseconds was determined as adequate for an accurate and stable solution.

COMPARISON OF ANALYSIS AND TEST RESULTS

The responses calculated by VecTor2 were rigorously compared to the measured responses of the test specimens. For brevity, only comparisons for mid-span displacements and crack profiles will be presented here. More detailed comparisons can be found at Saatci (2007). Figure 19 compares the mid-span displacements measured during the test with those calculated from the finite element analyses, for the first impact tests on undamaged specimens. The comparison for SS0b-1 is not included, since this specimen suffered extensive damage beyond the analysis capabilities of VecTor2. As seen in Figure 19, NLFEA predictions for the mid-span displacements of the test specimens were quite successful. Peak displacements were captured with considerable accuracy. However, some discrepancies were also observed at the post-peak vibrations. For example, for most tests, the analyses predicted a somewhat shorter period of vibration compared to the test measurements. Damping for the specimens was underestimated in some lightly-damaged specimens (a-series) resulting in higher calculated displacement amplitudes, whereas it was overestimated for all heavily-damaged specimens (b-series). On the other hand, peak displacements and post-peak vibrational periods were captured with greater accuracy for b-series specimens. In addition, residual displacements after the vibrations ceased were also captured accurately for all specimens.

For all analyses, crack profiles calculated by VecTor2 were visualized by a post-processor program called Augustus (Bentz 2003). Calculated and observed crack profiles and crack widths for two tests, a heavily damaged specimen and a lightly damaged specimen, are compared in Figures 20 and 21, respectively. It should be noted that, as a result of DSFM's rotating crack approach, crack direction at a load stage is determined by the principal axis of stress calculated for that load stage. In other words, the direction of cracks constantly changes, and VecTor2 does not report the crack directions of the preceding load stages in the output. Therefore, a crack profile as drawn by Augustus does not reflect the cracking history of the structure, but rather belongs only to that particular load stage. For this reason, several load stages need to be examined for a complete analysis of the estimated crack profile. Moreover, the crack condition is calculated for each concrete element, whereas the cracks in the specimen would develop singly over a region. Hence, the calculated crack directions for individual elements should be regarded as an estimate of the inclination and width of a typical crack over that region. In Figures 20 and 21, the crack profiles estimated at the initial stages of the response (negative moment phase), at the time the peak mid-span displacement occurred, and at the final resting stage of the specimen are presented and compared with the crack maps obtained from the test results. Note that the crack widths measured after the tests relate to the final resting stage of the specimen.

As seen in the figures, generally the crack profiles were predicted well. Vertical cracks starting from the top face were predicted correctly at the early stages of the response. Vertical cracks at the overhanging part and their slight inclination towards the supports were also predicted accurately. The analyses support the idea that these cracks occur at the very early stages of the response, as argued previously. In the later stages of the response, the

formations of diagonal shear cracks were accurately predicted in both flexural-critical and shear-critical specimens. Shear plug formations were also correctly represented in all heavily damaged specimens. However, some discrepancies, particularly for the crack widths below the impact point, were also observed, possibly due to the deficiencies of the behavioral models used under high strain rate conditions.

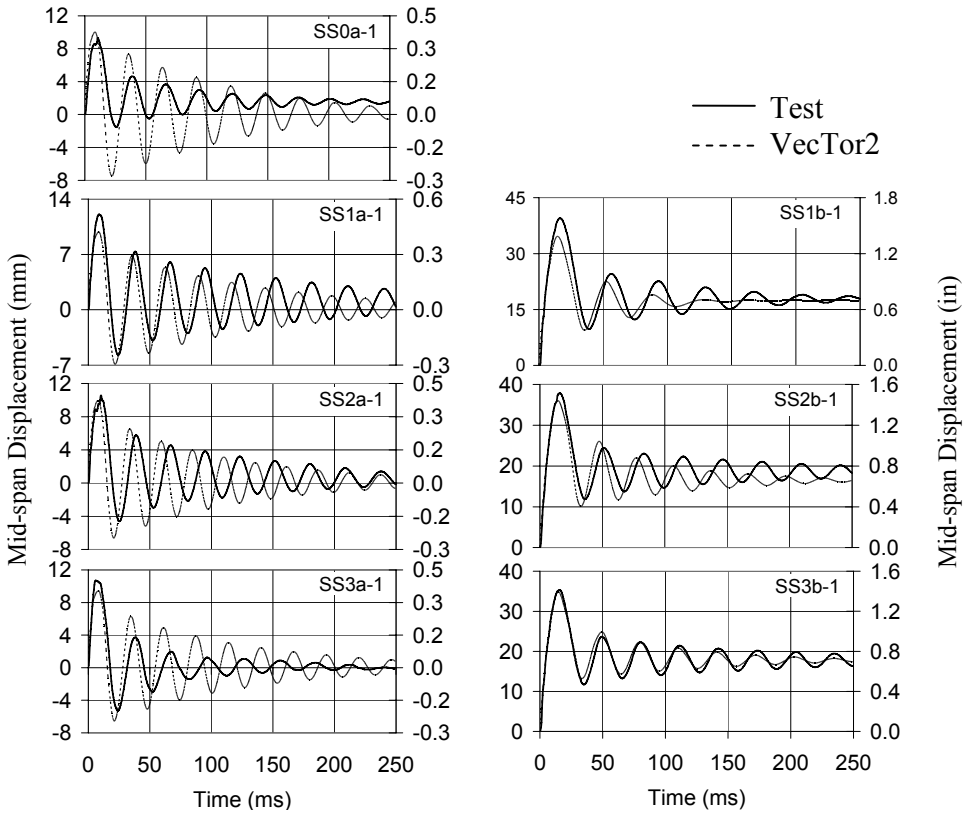

Figure 19 - Comparison of mid-span displacements for the first impacts on undamaged specimens

VecTor2 has the capability of restarting an analysis from the damaged condition of a previous analysis. In such an analysis, the displacements, strains, and crack conditions found at the last step of the previous analysis are taken as the initial condition of the new analysis, and new loads can be applied. Using this feature of the program, the second impact tests on the damaged specimens were modeled using the results of the first analyses. In Figure 22, mid-span displacements obtained from the analysis of the second impacts on damaged specimens were compared to the values obtained from the test. As seen in the figure, the estimates for peak and residual displacements were quite successful. Discrepancies in the post-peak vibrations exist, similar to those observed in the first impacts. The calculated response dampened out more quickly compared to the test responses, indicating a higher level of damping effective within in the analyses.

The crack profiles calculated by VecTor2 are compared in Figures 23 and 24 with the profiles obtained from the second tests. Only the results for two tests, SS3a-2 representing a lightly damaged specimen and SS2b-2 representing a heavily damaged specimen, are presented here for brevity. As seen in the figures, the analyses predicted general crack patterns reasonably well. Extensive cracking at the level of bottom reinforcement was predicted accurately; note that most specimens either developed horizontal cracks at this level, or they suffered spalling of the bottom cover concrete. Wide diagonal cracks forming the shear-plug were also predicted successfully, including the statically flexural-critical specimens. In the tests, it was observed that the diagonal cracks forming the shear-plug were wider close to the bottom; this also was observed in the calculations. However, some discrepancies exist in the crack width predictions. For example, VecTor2 over-estimated the residual widths of the vertical cracks at the mid-span.

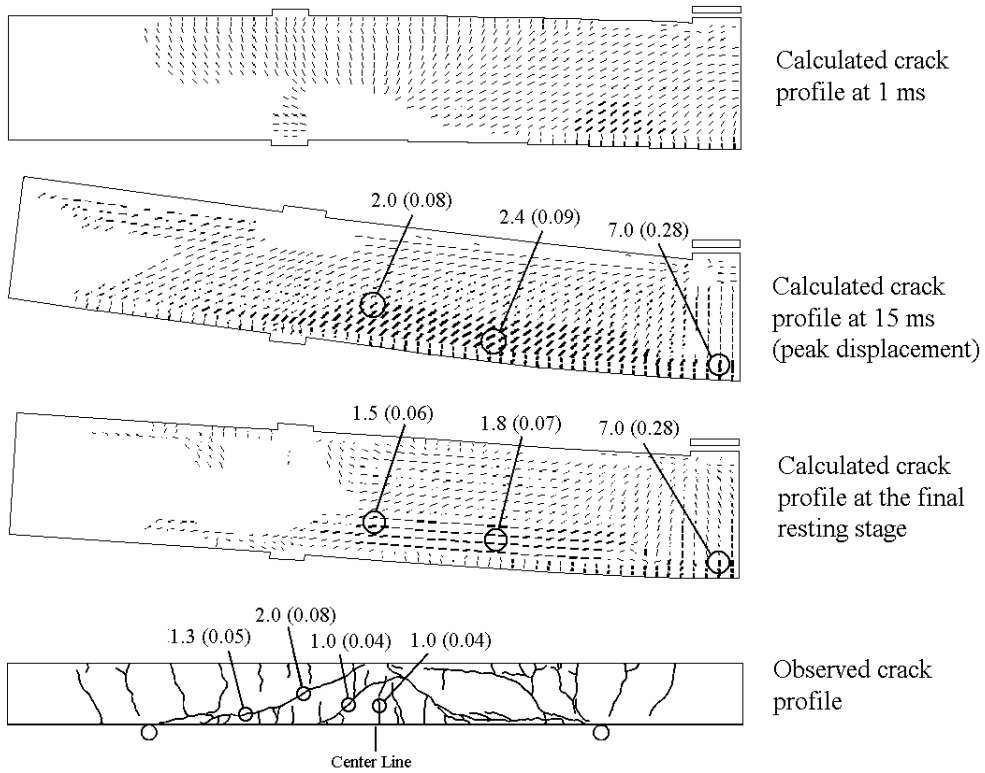

Figure 20 - Observed and calculated crack profiles, SS1b-1 [Crack widths: mm (in)]

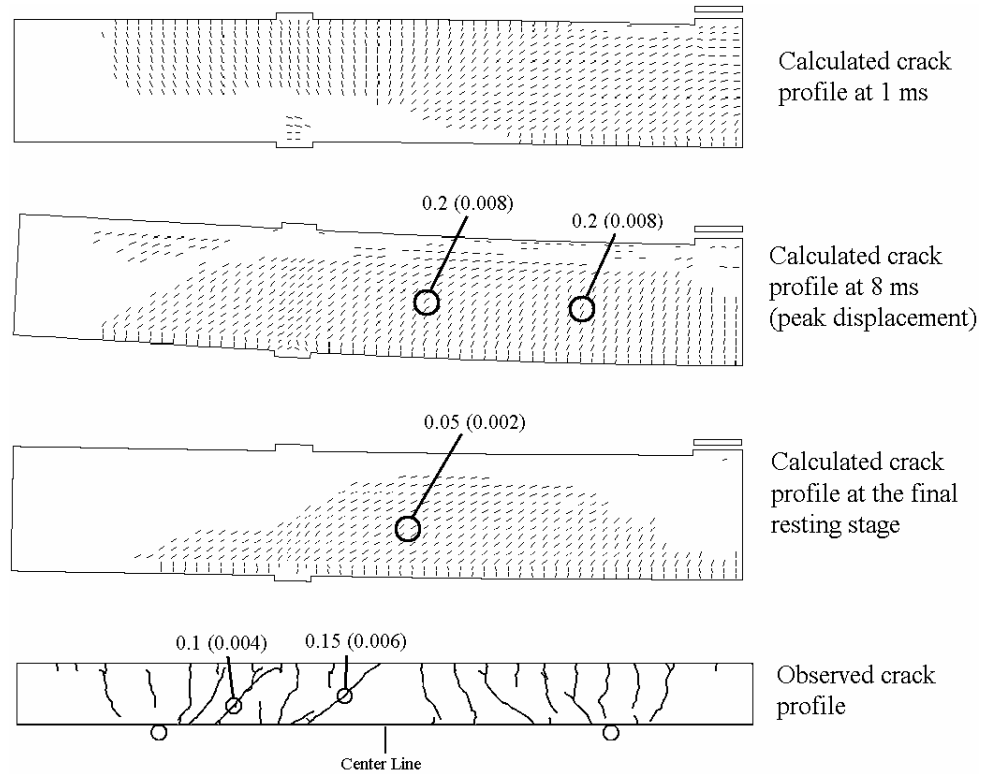

Figure 21 - Observed and calculated crack profiles, SS3a-1 [Crack widths: mm (in)]

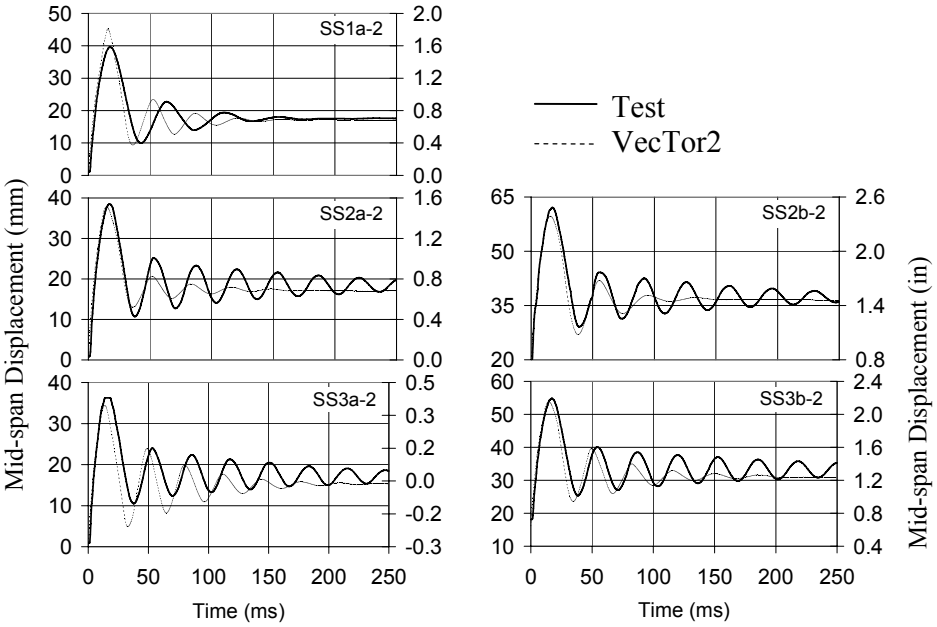

Figure 22 - Comparison of mid-span displacements for the second impacts on damaged specimens

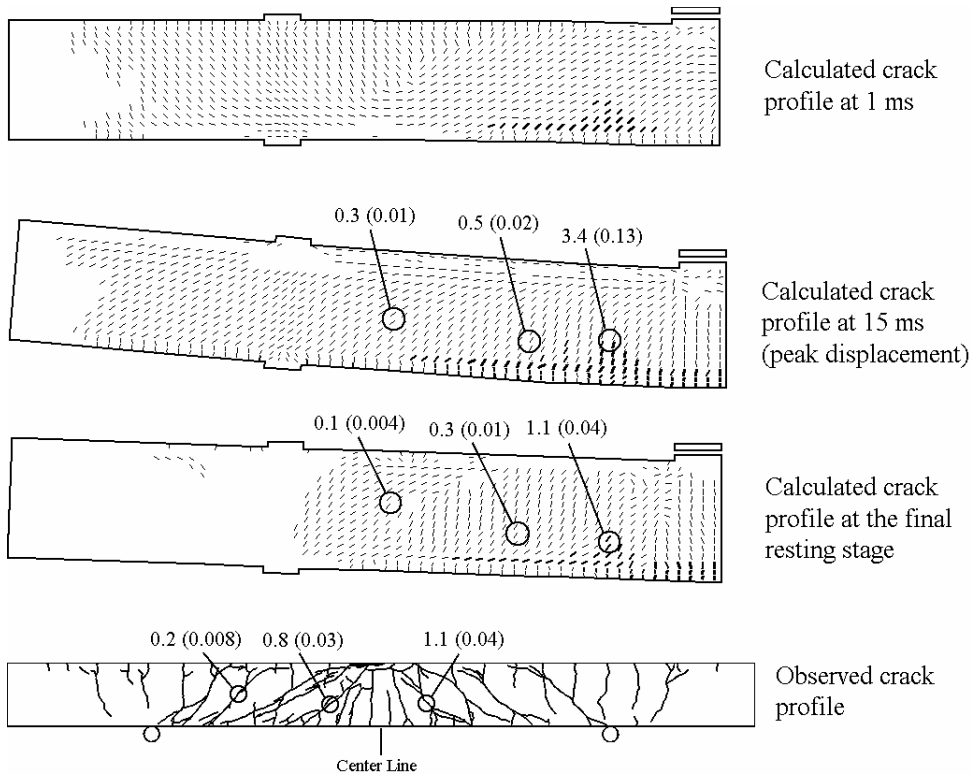

Figure 23 - Observed and calculated crack profiles, SS3a-2 [Crack widths: mm (in)]

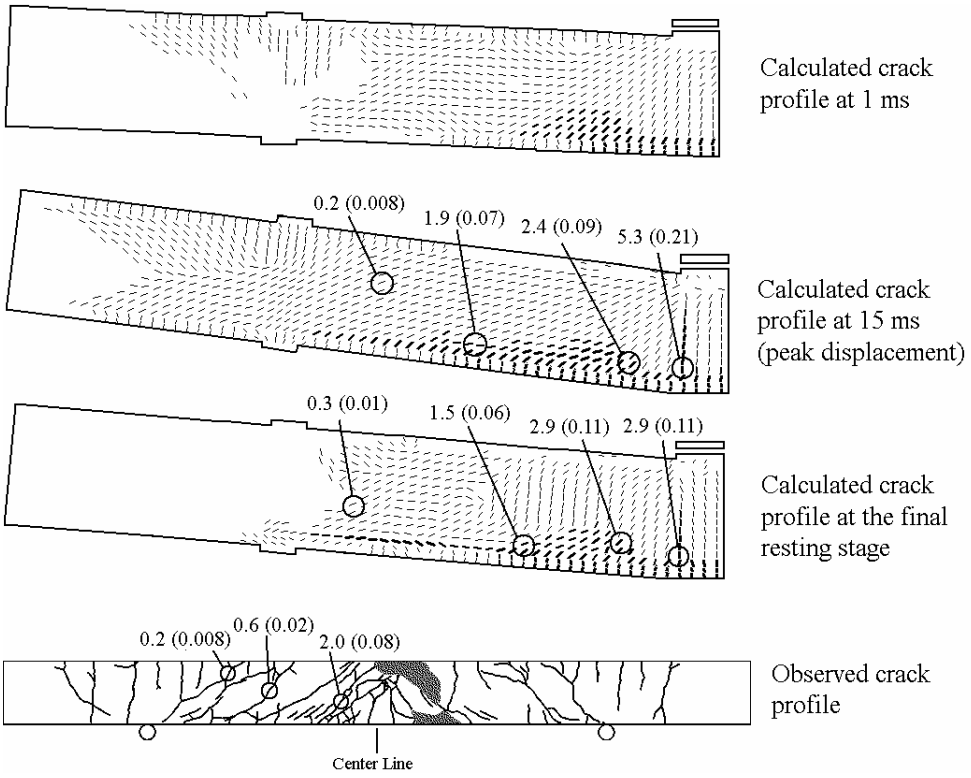

Figure 24 - Observed and calculated crack profiles, SS2b-2 [Crack widths: mm (in)]

CONCLUSIONS

The test program showed that the shear characteristics of the specimens played an important role in their overall behavior. All specimens, regardless of their shear capacity, developed severe diagonal shear cracks, forming a shear-plug under the impact point. Because of the highly dynamic nature of the responses, impact forces at the initial stages of response were mainly resisted by the inertia of the specimens, before the forces reached the supports. Therefore, the mass and geometric properties of a structure, such as the span length of a beam, are important factors in resisting the impact forces. In other words, it is not possible to estimate the impact capacity of a beam accurately based only on its cross-sectional properties

The proposed NLFEA methodology based on the DSFM performed well predicting the response of the test specimens. The shear-critical behaviors of the specimens were captured with high levels of accuracy. However, calculated post-peak vibrations showed some discrepancies compared to the test results, which can be attributed to the deficiencies regarding the modeling of the hysteretic behavior of concrete and steel under high strain rate conditions. Second impacts on damaged specimens were modeled successfully, indicating that the proposed methodology is applicable to the case of heavily-damaged structures. The simple approach followed for modeling the drop-weight and impact load was also successful, completely eliminating the need for an impact force- time history, and requiring only the mass and contact velocity of the impact weight. The methodology successfully modeled the damping behavior as well. The majority of the energy dissipating mechanisms was introduced through material models employed, such as the hysteresis rules, and only a small amount of viscous damping was needed to stabilize the solutions. The amount of viscous damping required was determined with a parametric study searching for the minimum amount needed for a stable solution, with no comparison or calibration with the test results. Hence, the role of an uncertain parameter in the model was minimized.

REFERENCES

Bentz, E. C., 2003, *Augustus: Finite Element Post-processor for VecTor2 and TRIX*, University of Toronto, Toronto, Canada.

Chopra, A. K., 2001, *Dynamics of Structures*, Prentice Hall, Inc., New Jersey.

Comité Euro-International du Béton (CEB), 1988, *Concrete Structures under Impact and Impulsive Loading*, Bulletin D'Information, No. 187.

Feldman, A.; Keenan, W. A.; and Siess, C. P., 1962, "Investigation of resistance and behavior of reinforced concrete members subjected to dynamic loading, Part III," *A Technical Report to The Office of the Chief of Engineers Department of the Army*, DASA-1259, 1962, University of Illinois, Urbana-Champaign.

Ho, D., 2004, "Impact response of reinforced concrete: An experimental and numerical investigation," M.A.Sc. Thesis, University of Toronto, Department of Civil Engineering.

Kishi, N.; Mikami, H.; Matsuoka, K.G.; and Ando, T., 2002, "Impact behavior of shear-failure-type RC beams without shear rebar," *International Journal of Impact Engineering*, Vol.27, pp.955-968.

May, I. M.; Chen, Y.; Roger, D.; Owen, J.; Feng, Y. T.; and Bere, A. T., 2005, "Behaviour of reinforced concrete beams and slabs under drop-weight impact loads," *Proceedings of the 6th Asia-Pacific Conference on Shock and Impact Loads on Structures*, Perth, W.Australia, pp.375-382.

Newmark, N. M., 1959, "A method of computation for structural dynamics," *Journal of the Engineering Mechanics Division*, ASCE, Vol.85, pp.67-94.

Palermo, D., and Vecchio, F. J., 2003, "Compression Field Modelling of Reinforced Concrete Subjected to Reversed Loading: Formulation," *ACI Structural Journal*, Vol. 100, No. 5, pp. 616-625.

Popovics, S., 1973, "A Numerical Approach to the Complete Stress-Strain Curve of Concrete," *Cement and Concrete Research*, Vol. 3, No. 5, pp. 583-599.

Saatci, S., 2007, "Behaviour and modelling of reinforced concrete structures subjected to impact loading," Ph.D. thesis, University of Toronto, Department of Civil Engineering.

Saatci, S., and Vecchio, F. J., 2009a, "Effects of Shear Mechanisms on Impact Behavior of Reinforced Concrete Beams," *ACI Structural Journal*, Vol. 106, No.1, pp. 78-86.

Saatci, S. and Vecchio, F. J., 2009b, "Nonlinear finite element modeling of reinforced concrete structures under impact loads," *ACI Structural Journal,* Vol. 106, No. 5, pp. 717-725.

University of Toronto - VecTor Analysis Group website: http://www.civ.utoronto.ca/vector

Vecchio, F. J., 2000, "Disturbed Stress Field Model for Reinforced Concrete: Formulation," *Journal of Structural Engineering*, Vol. 126, No. 9, pp.1070-1077.

Vecchio, F. J., and Wong, P., 2002, *VecTor2 and Formworks Manual*, University of Toronto, Department of Civil Engineering Publication, Publication No.2002-02.